

Numerical Study on Anomalous Heating over Apollo CM Test Model in Free-Piston Shock Tunnel Hiest

Tomoaki Ishihara^{*}
Yousuke Ogino[†]
Naofumi Ohnishi[‡]
Keisuke Sawada[§]
Hideyuki Tanno[¶]

^{*†‡}Tohoku University, 6-6-01 Aramaki-Aza-Aoba, Aoba-ku, Sendai, Miyagi, 980-8579, Japan

^{*}ishihara@cfm.mech.tohoku.ac.jp, [†]yogi@cfm.mech.tohoku.ac.jp, [‡]ohnishi@rhd.mech.tohoku.ac.jp,

[§]sawada@cfm.mech.tohoku.ac.jp

[¶]Japan Aerospace Exploration Agency, Kakuda Space Center, 1 Koganezawa, Kimigaya, Kakuda, Miyagi, 981-1525, Japan
tanno.hideyuki@jaxa.jp

Abstract

Aeroheating measurements on the Apollo CM test model placed in the free-piston shock tunnel Hiest was conducted. Although the convective heat flux distributions along wall surface normalized by a product of Stanton number and the square root of the Reynolds number should fall on a single curve for laminar flow case, the measured data for high enthalpy conditions resulted in significantly larger than one for low enthalpy conditions. In the Hiest experiment, stagnation heat fluxes on small probes were also measured. We could find that the anomalous heating phenomena are not shown for small test model but for large one that is called the scaling effect of anomalous heating phenomena. Similar tendencies were also observed at other shock tunnels: NASA Ames 42-Inch Shock Tunnel, Caltec T5, and CUBRC LENS. The cause for those anomalous heating phenomena is yet unknown. Anomalous heating poses a critical issue over the existing design method of thermal protection system for entry capsules. To clarify the cause of it, we numerically investigate these two factors: The radiative heat transfer in the shock layer and the radiation heating from the driver gas. From the results of our computations, radiative heating from shock layer was negligibly small. While, obtained total heat flux considering radiative heating from driver gas agreed well with measured heat flux. Scaling effect of the anomalous heating phenomena was also explained by accounting for the radiation from the driver gas. Therefore, we can say that the radiative heating from the driver gas may be the cause of those phenomena.

Key words: hypersonic flow, aerodynamic heating, shock tunnel

Introduction

NASA decided the retirement of space shuttles in July, 2011 due to enormous maintenance costs and safety defects, and announced Multi-Purpose Crew Vehicle (MPCV) concept as the next-generation manned space vehicle. MPCV is an Apollo-like space capsule which aims human explorations of the moon and Mars. Space capsules such as MPCV are now paid attention to, in the future, will play the principal role. When such a space capsule enters into the atmosphere of a planet, a strong shock wave is formed around the capsule, and it is exposed to severe aerodynamic heating in the shock layer. To protect the capsule from such heating environment, appropriate thermal protection system must be equipped. Therefore, it is critical to predict the heat fluxes accurately for the design of space capsules.

The free-piston shock tunnel, Hiest shown in Fig. 1, can produce test flow at stagnation pressure up to 150 MPa and at stagnation enthalpy up to 25 MJ/kg. Recently, aerodynamic heating on the Apollo command-module AS-202 test model illustrated in Fig. 2 placed in Hiest was measured by Tanno et al. [1, 2] The model was 6.4% scaled AS-202 command model made of SUS 304 stainless steel and had a diameter of 250 mm. To measure heat flux around the model, 84 miniature co-axial thermocouples were mounted on the forebody. Table 1 summarizes the upstream conditions of the test section determined by an axi-symmetric nozzle code [3]. The heat flux data were normalized by a product of Stanton number and the square-root of the Reynolds number in order to compare the Hiest heat flux data with the results obtained in other tunnel facilities and flight test. Measured heat flux with calculated one by thermochemical nonequilibrium calculation are summarized along the centerline of the model for AOA 30 deg. as shown in Fig. 3. The convective heat flux distributions along wall surface normalized by $St \times (Re_{\infty,D})^{1/2}$ should fall on a single curve for laminar flow case. We can confirm that calculated one normalized by $St \times (Re_{\infty,D})^{1/2}$ are almost same for all the cases. On the other hand, the measured data for high enthalpy condition resulted in larger than those for low enthalpy condition and measured values are considerably higher than calculated convective ones for all conditions. Such anomalous heating phenomena obviously pose a critical issue over the existing design method of thermal protection system for entry capsules.

Additionally, in Hiest experiment, stagnation heat fluxes on small probes also measured [4]. Figure 4-(a) and (b) show the configurations of the probes which have the base radius $\Phi = 20$ and $\Phi = 50$ mm, respectively. The $\Phi 20$ probe has the nose radius $R = 10$ or $R = 50$ mm. The $\Phi 50$ probe has $R = 100$ mm. Figure 5 shows the normalized stagnation heat flux for each probe with the results of Apollo CM test model ($\Phi = 250$ mm, $R = 300$ mm). The heat flux measured in Hiest is normalized by calculated convective heat flux at stagnation point. Freestream parameters are summarized in Tab. 2. For $\Phi 20R10$ and $\Phi 20R50$ probes, we can see that the values are from 1.0 to 1.3. While, for $\Phi 50R100$ probe and Apollo CM test model, the values are over 1.4. This means that there are large discrepancies between measured heat flux and calculated convective one. The anomalous heating phenomena are not shown for small test model but for large one.

Anomalous heating phenomena were also observed at other shock tunnels; NASA Ames 42-Inch Shock Tunnel [5], Caltec T5 [6, 7, 8], CUBRC LENS I [9, 10]. From these literatures, large discrepancies between calculated convective heat flux by LAURA [11, 12] or DPLR [13, 14] codes and measured heat flux by each shock tunnel were confirmed. For instance, in Ref. [6], the effect of turbulence heat transport was investigated to examine the cause of those discrepancies. Comparison of T5 data with the calculated heating rate by DPLR accounting for turbulence was performed. As a result, measured profiles were not explained by only turbulence transport.

As the cause of anomalous heating phenomena, we focus on radiative heating from driver gas. In Hiest experiments, the driver gas is compressed by a heavy piston, then the pressure and temperature in the compression tube rise up. When diaphragms rupture, remarkable luminosities are observed, therefore, the intense radiation from the driver gas can be the cause for anomalous heating. Since the driver gas is compressed in other shock tunnels as with Hiest, this phenomena can occur not only in Hiest but also in other shock tunnels. In this study, we compute the flowfield over the forebody of the Apollo CM test model and evaluate the convective and radiative heat fluxes on the model surface. The heat flux on small probes are also calculated to examine the scaling effect of anomalous heating. In order to clarify the cause of anomalous heating, we examine the radiative heating both from the shock layer and the driver gas.

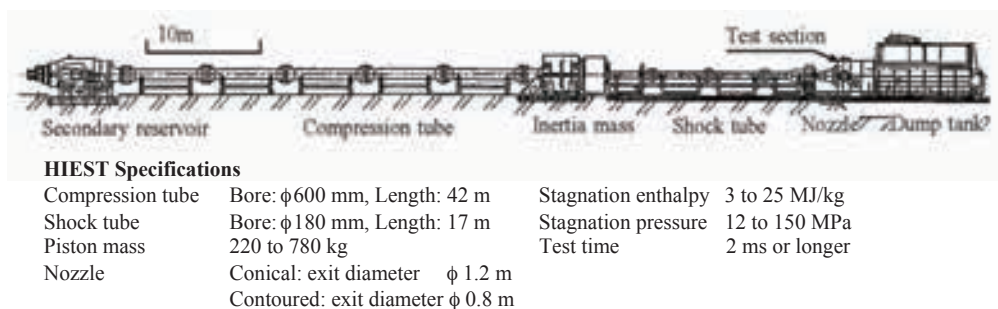


Figure 1. Free-piston shock tunnel Hiest [1].

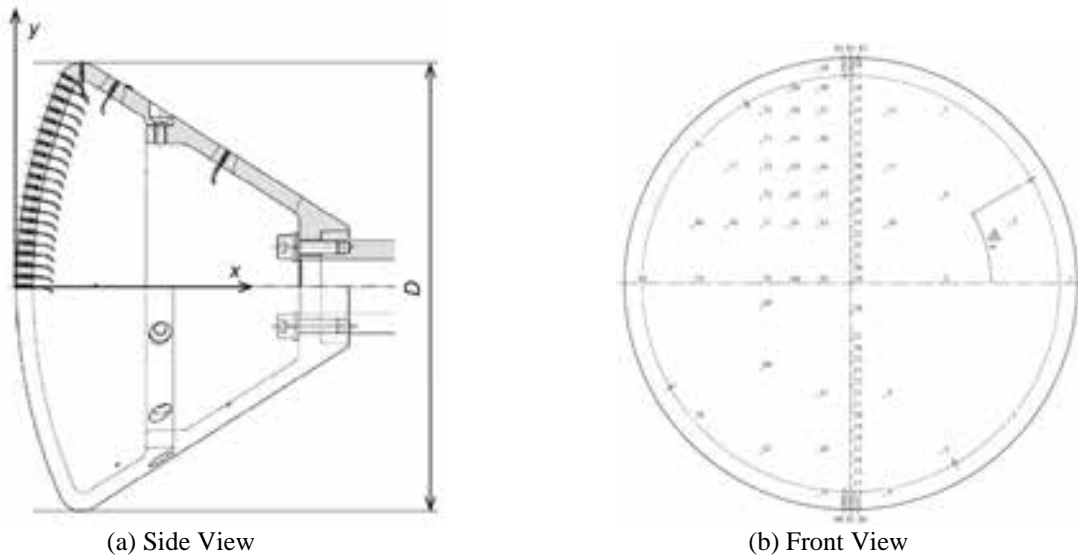


Figure 2. Apollo CM test model [1].

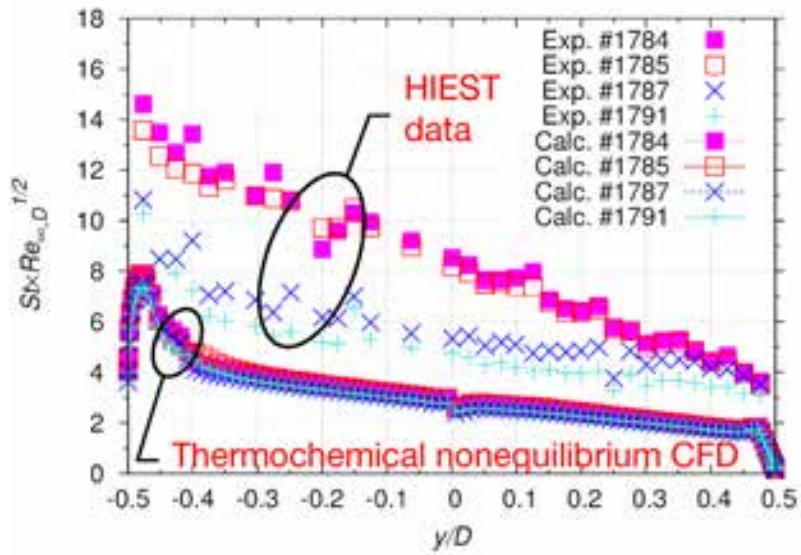


Figure 3. Measured heat flux distribution along the centerline of the model.

Table 1. Freestream parameters of Apollo CM test campaign at Hiest calculated by JAXA in-house code.

Shot #	H_0 [MJ/kg]	P_0 [MPa]	T_{∞} [K]	$T_{v\infty}$ [K]	ρ_{∞} [kg/m ³]	V_{∞} [m/s]	M_{∞}	Re_{∞} × 10 ⁶ [1/m]
1784	19.554	57.401	2035.2	2038.2	0.01457	5507.3	5.909	1.167
1785	21.059	55.060	2143.0	2146.8	0.01315	5690.2	5.885	1.050
1787	8.094	49.700	841.7	849.5	0.02643	3729.1	6.496	2.595
1791	6.759	30.750	649.7	668.1	0.01919	3420.8	6.739	2.060

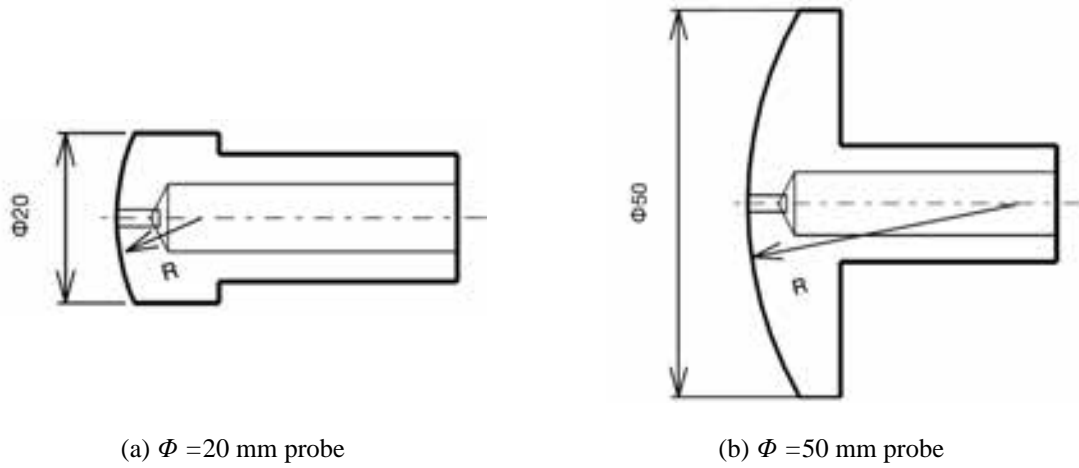
(a) $\Phi = 20$ mm probe(b) $\Phi = 50$ mm probe

Figure 4. Schematic of small probes.

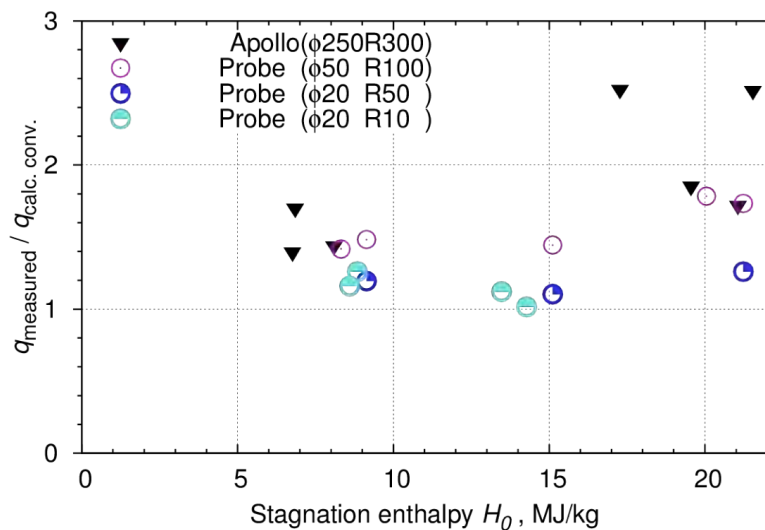


Figure 5. Scaling effect of the anomalous heating phenomena.

Table 2. Freestream parameters of small probes campaign in HIEST calculated by JAXA in-house code.

Shot #	Test gas	Test model [mm]	H_0 [MJ/kg]	P_0 [MPa]	$T_{f\infty}$ [K]	$T_{w\infty}$ [K]	ρ_∞ [kg/m ³]	V_∞ [m/s]	M_∞	Re_∞ $\times 10^6$ [1/m]
1886	Air	$\Phi 20 R10$	13.471	47.906	1455.9	1461.8	0.01633	4665.8	6.108	1.443
1887	Air	$\Phi 20 R10$	11.326	49.102	1242.8	1249.3	0.01942	4327.5	6.190	1.762
1888	N ₂	$\Phi 20 R10$	14.276	48.996	1243.7	3169.2	0.01467	4934.5	7.021	1.407
1889	Air	$\Phi 20 R10$	8.596	54.634	908.7	915.8	0.02717	3835.8	6.440	2.640
1890	N ₂	$\Phi 20 R10$	8.845	55.530	614.8	2581.9	0.02293	3950.1	7.867	2.733
1891	Air	$\Phi 50$	8.318	52.841	869.9	877.3	0.02702	3778.5	6.479	2.663
1893	Air	$\Phi 50$	20.048	42.506	1946.4	1952.3	0.01050	5551.9	6.013	0.920
1894	N ₂	$\Phi 20 R50, \Phi 50$	21.232	43.941	2261.4	3563.4	0.01026	5785.3	6.036	0.867
1895	N ₂	$\Phi 20 R50, \Phi 50$	15.112	48.230	1359.8	3231.9	0.01397	5055.6	6.882	1.306
1896	N ₂	$\Phi 20 R50, \Phi 50$	9.140	57.726	643.5	2606.8	0.02324	4014.4	7.824	2.728

Numerical Methods

The numerical method is based on the cell-center finite volume discretization. For calculation of flowfield over Apollo CM test model, we solve the three-dimensional Navier-Stokes equations accounting for thermochemical nonequilibrium in the shock layer. On the other hand, for small probes, we solve the axi-symmetric ones. We employ Park's two-temperature thermochemical model [15] in which five chemical species (O, N, NO, N₂, O₂) are considered. The convective numerical flux is calculated by SLAU [16]. We employ MUSCL approach [17] for attaining a second order spatial accuracy. In the time integration, we use the LU-SGS implicit method [18] and Euler explicit method, for computation of flowfield over Apollo CM test model and small probes, respectively. To improve the stability in the integration of source terms, the diagonal point implicit method [19] is utilized.

The radiative transfer equation is solved one-dimensionally in the direction normal to the wall [20]. The absorption coefficients are calculated using the multi-band model [21]. O, N, NO, O₂, and N₂ are considered as contributors to radiation. Absorption coefficients of each contributor are evaluated at 10,000 wavelength points. They are constructed for the wavelength region from 750 to 15,000 Å. In this numerical work, radiative heat transfer calculation is uncoupled with flowfield.

Numerical Conditions

Freestream conditions for aeroheating measurements on Apollo CM test model and small probes equal to experimental value in Tab. 1 and 2, respectively. We compute the four typical conditions: Shot # 1785, 1791, 1889, 1891. Mass fractions of freestream calculated by NENZF [22] are listed in Tab. 3 and 4. We assume that wall boundary condition is isothermal and fully-catalytic wall.

We generate grids adapted to the shock wave front to estimate heat flux appropriately [23]. A typical example of the computational grid for Apollo CM test model, shown in Fig. 6, has 51 points in the wall normal direction and in the direction along the wall and 65 points in circumferential direction. Figure 7 shows grids for $\Phi 20R50$ and $\Phi 50R100$ probes. Since we are interested in the only stagnation heat flux, the configuration of afterbody is simplified. There are 51 grid points in the wall normal direction and 101 points in the direction along the wall. The distance between the first layer and the wall surface, that means grid resolution for temperature boundary layer, is determined from grid convergence property of convective heat flux.

Table 3. Mass fraction of freestream in Apollo CM test campaign.

Shot #	$C_{O_{\infty}}$	$C_{N_{\infty}}$	$C_{NO_{\infty}}$	$C_{O_{2\infty}}$	$C_{N_{2\infty}}$
1785	1.308×10^{-1}	4.514×10^{-6}	3.600×10^{-2}	8.326×10^{-2}	7.500×10^{-1}
1791	2.397×10^{-3}	4.399×10^{-12}	5.931×10^{-2}	2.009×10^{-1}	7.373×10^{-1}

Table 4. Mass fraction of freestream in small probes campaign.

Shot #	$C_{O_{\infty}}$	$C_{N_{\infty}}$	$C_{NO_{\infty}}$	$C_{O_{2\infty}}$	$C_{N_{2\infty}}$
1889	4.785×10^{-3}	5.819×10^{-12}	6.054×10^{-2}	1.979×10^{-1}	7.368×10^{-1}
1891	4.139×10^{-3}	4.738×10^{-12}	6.038×10^{-2}	1.986×10^{-1}	7.368×10^{-1}

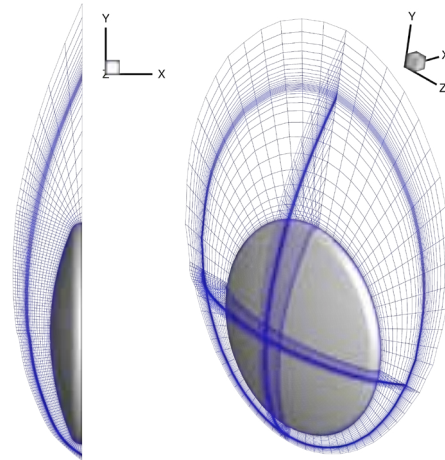
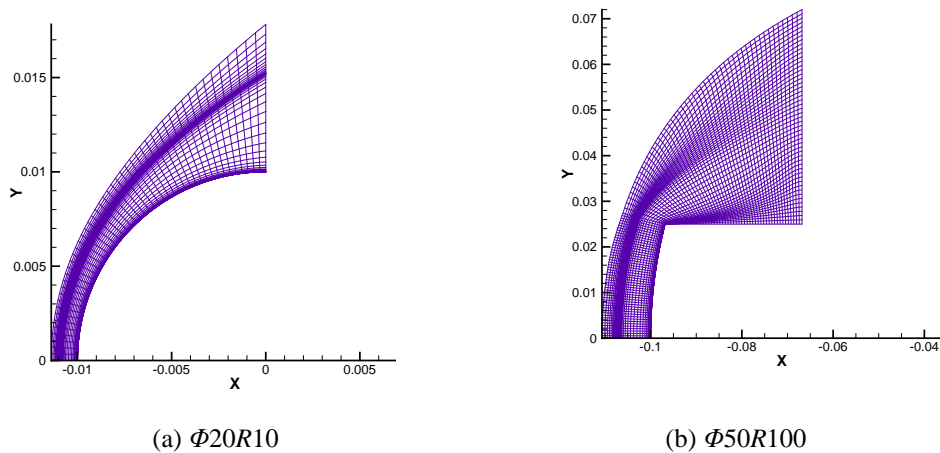


Figure 6. Solution-adaptive grids for Apollo CM test model.



(a) $\Phi 20R10$

(b) $\Phi 50R100$

Figure 7. Solution-adaptive grids for small probes.

Results and Discussion

Effects of Radiative Heat Flux

When the radiative heating from driver gas is considered, we simply regard the driver gas as a black body, and set the Plank function B_λ as a boundary of the radiative heat transfer equation in the shock layer. Since the driver gas temperature was not able to measure due to experimental constraints, we assume a certain driver gas temperature T_{est} at which calculated heat flux agree well with experimental one.

Figure 8 shows normalized total heat flux including radiative heating from driver gas for Shot # 1791 (low enthalpy condition) and Shot # 1785 (high enthalpy condition). Asterisk-shaped symbols show the baseline convective heat flux profile. While, open-square symbols show the sum of the convective heat flux and radiative heat flux from the shock layer. Total heat fluxes including radiation from driver gas are indicated cross-shaped symbols. Radiative heat flux from the shock layer is negligibly small both for conditions. For Shot # 1791, as shown in Fig. 8-(a), we could obtain a good agreement with Hiest heat flux data, if we assume the temperature of the driver gas T_{est} to be 2,700 K. For Shot # 1785, as shown in Fig. 8-(b), we obtain a reasonable agreement with Hiest heat flux data, if we assume the temperature of the driver gas T_{est} to be 4,500 K. One can find that

the radiation from driver gas greatly contributes to radiative heat flux to the wall surface. Since the temperature in shock layer is about 10,000 K at most even for higher enthalpy condition, then absorption coefficients are relatively small. Therefore, the radiative heating from driver gas is hardly absorbed in the shock layer and directly heats the test model.

Validation of the estimated temperature of the driver gas

We validate the driver gas temperature T_{est} at which we could obtain good agreement with measured data. In the HIEST experiment, it is hard to measure the driver gas temperature directly because of experimental configuration. We estimate the experimental temperature of driver gas assuming adiabatic compression given by following expression,

$$T_{\text{exp}} = \left(\frac{P_{\text{rup}}}{P_{\text{init}}} \right)^{\frac{\gamma-1}{\gamma}} \times T_{\text{init}}, \quad (1)$$

where P_{init} and T_{init} mean the pressure and temperature before compression, respectively. We set $P_{\text{init}} = 1,013$ hPa, and $T_{\text{init}} = 300$ K. P_{rup} which indicates the measured pressure when the first diaphragm ruptured is 85 MPa and 37 MPa for Shot # 1791 and Shot # 1785, respectively. Since driver gas is composed of He and Ar, we set $\gamma = 5/3$. Then, the temperature of the driver gas T_{exp} is 3,200 K and 4,400 K, respectively. For Shot # 1785, the T_{est} seems a reasonable assumption. While, for Shot # 1791, there are discrepancies between T_{est} and T_{exp} .

We estimated experimental driver gas temperature T_{exp} at which the first diaphragm ruptures. However, T_{exp} may change from the value at which the first diaphragm ruptures, since there is a time delay before measuring heat flux. Thus, we need to calculate flowfield in compression tube, shock tube and nozzle for accurate estimation of the experimental driver gas temperature T_{exp} . In addition, since spectroscopic measurement is carried out before too long, we will investigate the radiation from driver gas in more detail.

Scaling Effect of Anomalous Heating Phenomena

Figure 9 shows the total heat flux distribution including radiative heating from the driver gas on $\Phi 20R10$ probe for Shot # 1886 and $\Phi 50R100$ probe for Shot # 1893. The stagnation enthalpy both for shots is comparable. Horizontal axis shows the distance from stagnation point. We assumed the driver gas temperature $T_{\text{est}} = 3,000$ K. In the case of $\Phi 20R10$ probe, we can find that convective heat flux is significantly larger than radiative heat flux. Since the ratio of radiative heat flux to convective heat flux is small, the anomalous heating phenomena are not shown notably. While, in the case of $\Phi 50R100$ probe, since the ratio of radiative heat flux to convective heat flux is not small, the anomalous heating phenomena are observed. Therefore, scaling effect of the anomalous heating phenomena is also explained by accounting for the radiation from the driver gas.

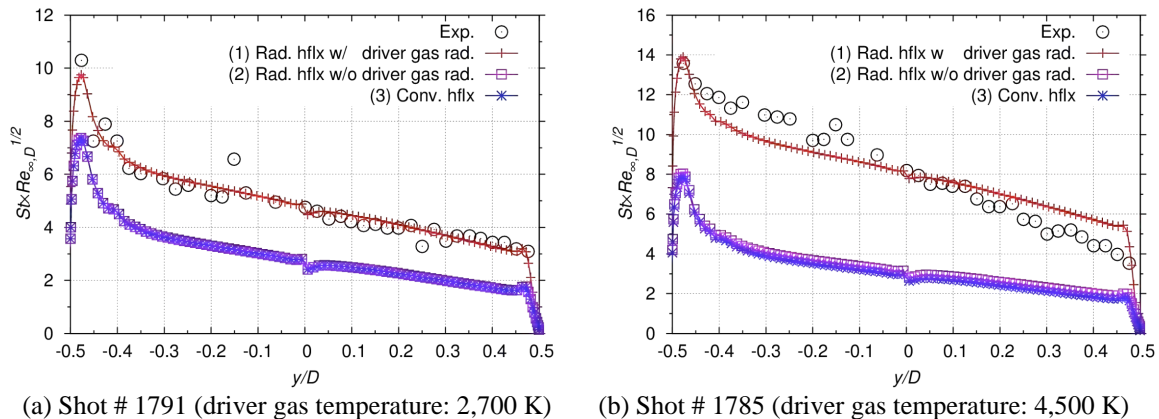


Figure 8. Normalized total heat flux including radiative heating from driver gas at AOA 30 deg.

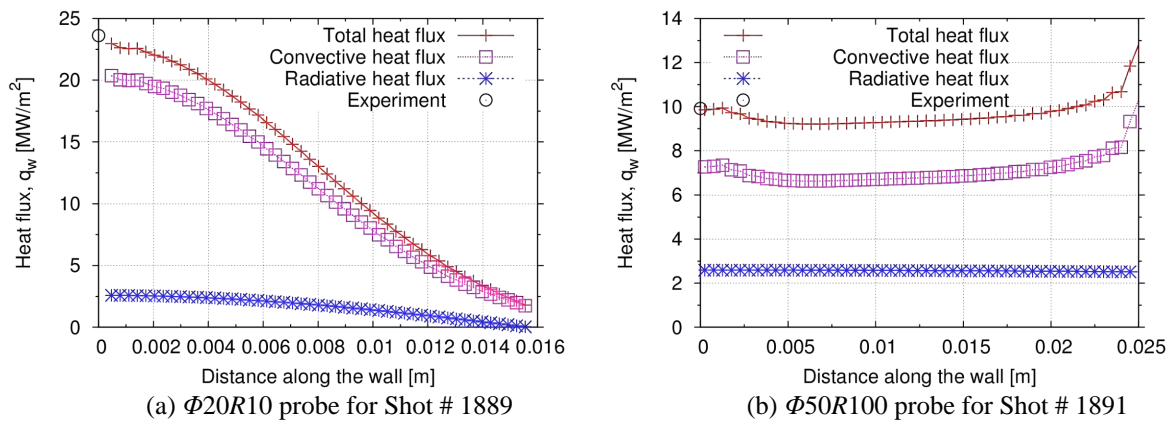


Figure 9. Total heat flux including radiative heating from the driver gas on small probes.

Summary

In this study, we computed heat fluxes for the forebody of Apollo CM test model to clarify the cause of the anomalous heating phenomena measured in Hiest experiments. We examined radiative heating both from the shock layer and the driver gas. It was found that Hiest heat flux data could be reproduced if radiative heating from the driver gas was included, with the temperature of the driver gas properly chosen. On the other hand, radiative heating from the shock layer was negligibly small.

We also examined the scaling effect of the anomalous heating phenomena. For probes, which had small radius, convective heat flux was significantly larger than radiative heat flux. Since the ratio of radiative heat flux to convective one was small, the anomalous heating phenomena were not shown notably. While, for probes which had large radius, the ratio of radiative heat flux to convective one was not small, such phenomena were shown. Scaling effect of the anomalous heating phenomena was also explained by accounting for the radiation from the driver gas.

Therefore, it is quite likely that anomalous heating phenomena seen in measured heat flux data are caused by radiative heating from the driver gas, although the further validation of driver gas temperature is needed. The anomalous heating phenomena in other shock tunnels also can be caused by the radiative heating from driver gas.

References

- [1] Tanno, H., Kodera, M., Komuro, T., Sato, K., Takahashi, M., and Itoh, K., "Aeroheating Measurements on a Reentry Capsule Model in Free-Piston Shock Tunnel Hiest," AIAA Paper 2010-1181, 2010.
- [2] Tanno, H., Komuro, T., Sato, K., Itoh, K., Yamada, T., Sato, N., and Nakano, E., "Heat Flux Measurement of Apollo Capsule Model in the Free-piston Shock Tunnel Hiest," AIAA Paper 2009-7304, 2009.
- [3] Takahashi, M., Kodera, M., Itoh, K., Sato, K., and Tanno, H., "Influence of Thermal Non-equilibrium on Nozzle Flow Condition of High Enthalpy Shock Tunnel Hiest," AIAA Paper 2009-7267, 2009.
- [4] Tanno, H., Komuro, T., Sato, K., Itoh, K., Ishihara, T., Ogino, Y., and Sawada, K. "Stagnation Heat Flux of Blunt Models in a High-Enthalpy Wind Tunnel," Conference proceedings of Symposium on SHOCK WAVES 1A1-2, 2012.
- [5] Stewart, D. A. and Chen, Y. K., "Hypersonic Convective Heat Transfer over 140-deg Blunt Cones in Different Gases," *Journal of Spacecraft and Rockets*, Vol.31, No. 5, pp.735-743, 1994.
- [6] Eric, M., Stuart, L., and Hans, G., "Apollo-Shaped Capsule Boundary Layer Transition at High-Entahlpy in T5," AIAA Paper 2010-446, 2010.

- [7] Wright, M. J., Olejniczak, J., Brown, J. L., Hornung, H. G., and Edquist, K. T., "Modeling of Shock Tunnel Aeroheating Data on the Mars Science Laboratory Aeroshell," *Journal of Thermophysics and Heat Transfer*, Vol. 20, No. 4, pp.641-651, 2006.
- [8] Olejniczak, J., Wright, M. J., Laurence, S., Hornung, H. G., and Edquist, K. T., "Computational Modeling of T5 Laminar and Turbulent Heating Data on Blunt Cones, Part I: Titan Applications," AIAA Paper 2005-0176, 2005.
- [9] Hollis, B. R., Liechty, D. S., Wright, M. J., Holden, M. S., Wadhams, T. P., MacLean, M., and Dyakonov, A., "Transition Onset and Turbulent Heating Measurements for the Mars Science Laboratory Entry Vehicle," AIAA Paper 2005-1437, 2005.
- [10] MacLean, M., Wadhams, T., Holden, M., and Hollis, B. R., "Investigation of Blunt Bodies with CO₂ Test Gas Including Catalytic Effects," AIAA Paper 2005-4693, 2005.
- [11] Gnoffo, P. A., "An Upwind Biased, Point-Implicit Relaxation Algorithm for Viscous, Compressible Perfect-Gas Flows," NASA TP-2953, 1990.
- [12] Mazaheri, Alireza, Gnoffo, P. A., Johnson, C. O., and Kleb, W., "LAURA Users Manual: 5.3-28528," NASA TM-2010-216386, 2010.
- [13] Wright, M. J., Candler, G. V., and Bose, D., "Data-Parallel Line Relaxation Method for the Navier-Stokes Equations," *AIAA Journal*, Vol. 36, No.9, pp.1603-1609, 1998.
- [14] Wright, M. J., White, T., and Mangini, N., "Data Parallel Line Relaxation (DPLR) Code User Manual Acadia-Version 4.01.1," NASA-TM-209-215388, 2009.
- [15] Park, C., *Nonequilibrium Hypersonic Aerothermodynamics*, John Wiley and Sons Inc., New York, 1989.
- [16] Kitamura, K. and Shima, E., "A New Pressure Flux for AUSM-Family Schemes for Hypersonic Heating Computations," AIAA Paper 2011-3056, 2011.
- [17] Van Leer, B., "Towards the Ultimate Conservation Difference Scheme. V. A Second-Order Sequel to Godunov's Method," *Journal of Computational Physics*, Vol. 32, No. 1, pp.101-136, 1979.
- [18] Yoon, S. and Jameson, A., "An LU-SSOR Scheme for the Euler and Navier-Stokes Equations," AIAA Paper 87-600, 1987.
- [19] Eberhardt, S. and Imlay, S., "Diagonal Implicit Scheme for Computing Flows with Finite Rate Chemistry," *Journal of Thermophysics and Heat Transfer*, Vol. 6, No. 2, pp. 208-216, 1992.
- [20] Vincenti, W. G. and Kruger, C. H., *Introduction of Physical Gas Dynamics*, John Wiley and Sons Inc., New York, 1967.
- [21] Park, C. and Milos, F. S., "Computational Equations for Radiating and Ablating Shock Layers," AIAA Paper 90-0356, 1990.
- [22] Lordi, J. A., Mates, R. E., and Mossele, J. R., "Computer Program for Numerical Solution of Nonequilibrium Expansions of Reacting Gas Mixtures," NASA CR-472, 1966.
- [23] Candler, G. V. and Nompelis, I., "Computation Fluid Dynamics for Atmospheric Entry," Von Karman Institute for Fluid Dynamics Lecture Series, RTO-EN-AVT-162, 2009.